

ARTICLE

DOI: 10.1038/s42005-018-0014-7

OPEN

Continuous-wave multiphoton photoemission from plasmonic nanostars

Murat Sivis¹, Nicolas Pazos-Perez², Renwen Yu³, Ramon Alvarez-Puebla^{2,4},
F. Javier García de Abajo^{3,4} & Claus Ropers¹

Highly nonlinear optical processes require high intensities, typically achieved with ultrashort laser pulses, and hence, they were first observed with the advent of picosecond laser technology. An alternative approach for reaching the required field intensities is offered by localized optical resonances in tailored plasmonic nanostructures, enabling the enhancement of a multitude of nonlinear phenomena. However, so far, plasmon-enhanced high-order nonlinear effects have been restricted to experiments involving short-pulsed and ultrafast laser sources. Here, we demonstrate localized three-photon photoemission from chemically synthesized plasmonic gold nanostars under continuous-wave illumination at sub-MWcm⁻² incident intensities. Intensity- and polarization-dependent measurements confirm the non-linearity of the photoemission process and agree with quantum mechanical calculations of the electron yield from nanostar tips with features smaller than 5 nm, which facilitate local intensity enhancement factors exceeding 1000. Our results open up new avenues for the design of accessible nanoscale coherent electron sources, with potential applications in microscopy, spectroscopy, sensing, and signal processing.

¹4th Physical Institute-Solids and Nanostructures, University of Göttingen, Göttingen 37077, Germany. ²Department of Physical Chemistry and EMaS, Universitat Rovira i Virgili, Carrer de Marcel·lí Domingo s/n, 43007 Tarragona, Spain. ³ICFO—Institut de Ciències Fotoniques, The Barcelona Institute of Science and Technology, Castelldefels, 08860 Barcelona, Spain. ⁴ICREA—Institució Catalana de Recerca i Estudis Avançats, Passeig Lluís Companys 23, 08010 Barcelona, Spain. Correspondence and requests for materials should be addressed to M.S. (email: murat.sivis@uni-goettingen.de) or to F.J.G.d.A. (email: javier.garciadeabajo@nanophotonics.es)

Nanoscale confinement of optical fields in plasmonic structures is accompanied by significant field enhancements that increase the strength of both linear and nonlinear phenomena, such as single-molecule Raman scattering^{1,2} and fluorescence³, harmonic generation^{4–10}, nanoplasma extreme-ultraviolet light generation^{9,11,12}, and multiphoton and strong-field photoemission^{13–23}. The latter has attracted much attention in experiments involving surfaces^{19–23}, resonant antennas¹⁸, or sharp metallic tips^{13–17}, facilitating the development of high-coherence tip-based laser-driven pulsed electron sources^{24–31} for time-resolved electron microscopy and diffraction^{32–34}.

In general, nonlinear optical signals can be enhanced by confining a given incident average power in time and/or space. While temporal confinement is ubiquitous in the use of ultrashort laser pulses, additional spatial confinement is realized in optical nanostructures, defining the field of ultrafast nano-optics^{35,36}. In particular, extensive theoretical and experimental work has led to a growing level of control over the near-field localization associated with resonant modes in optimized nanostructure geometries^{37,38}. Exceedingly large-field enhancements in plasmonic nanostructures suggest the observation of highly nonlinear

processes even under continuous-wave (CW) illumination conditions.

Here, we study nonlinear photoelectron emission from individual resonant gold nanostars under CW excitation at incident intensities below 1 MW cm^{-2} , using a 660-nm low-power (60 mW) laser diode. We characterize the CW multiphoton photoemission yield as a function of incident intensity and polarization, and further provide spatial scans to identify emission from individual nanostars. These findings are compared with photoemission measurements using 10 fs laser pulses at 800 nm central wavelength. Additionally, we present simulations of the electromagnetic near-field distributions and the resulting photoelectron yield that further support the nanoscale plasmonic origin of CW nonlinear photoemission at the single-particle level. Our results illustrate the potential of plasmonic field confinement in tailored resonant nanostructures to widely proliferate nonlinear nano-optics beyond ultrafast science.

Results

Nanostar sample preparation and optical properties. The nanostars used in our experiments are grown by a seed-mediated approach^{2,39} (see “Methods” for details) and exhibit multiple

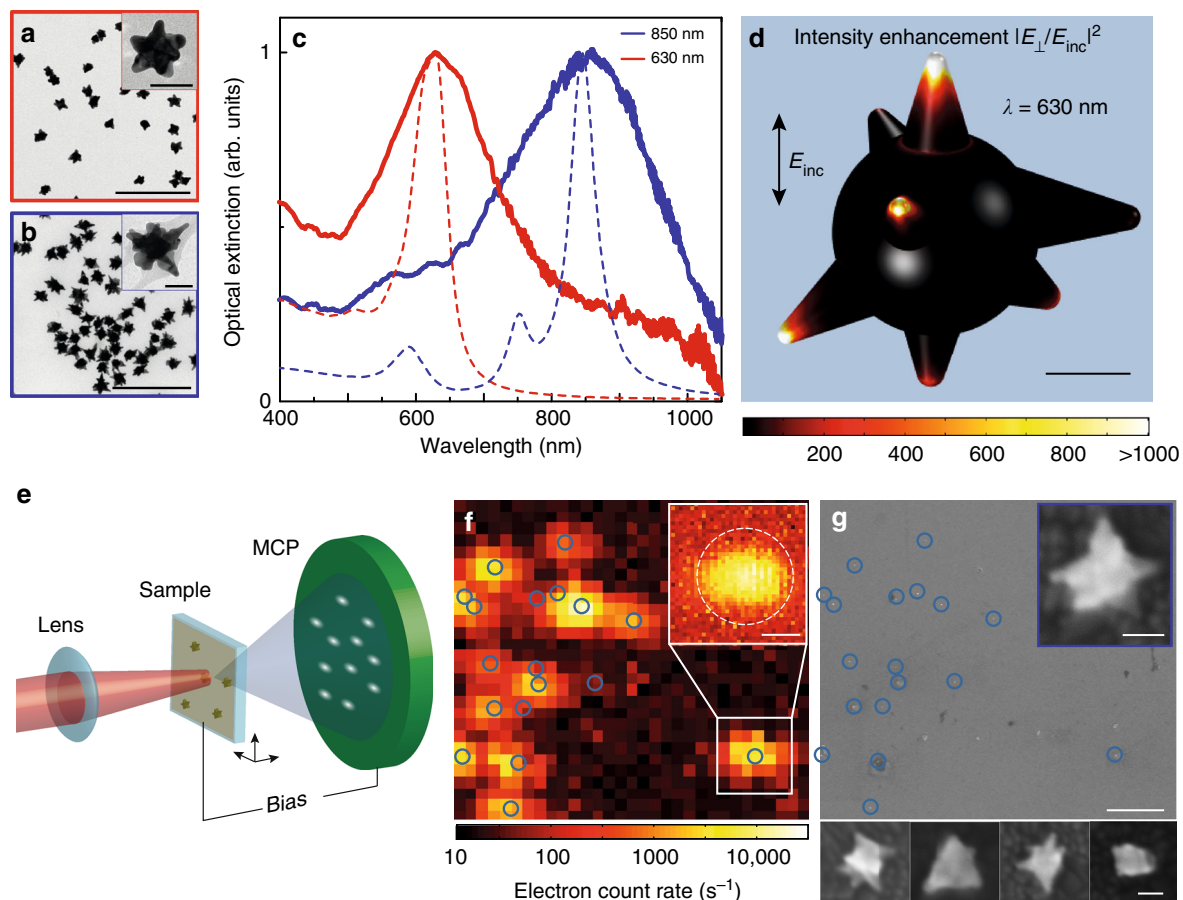


Fig. 1 Optical field enhancement and femtosecond photoemission in resonant nanostars. **a, b** TEM images of nanostars on Si_3N_4 membranes (500 nm scale bars). Insets show close-ups of single stars (50 nm scale bars). **c** Measured optical extinction spectra (solid lines) for ensembles of the two nanostar batches (see color-coded frames in **a, b**), compared to simulated spectra of individual nanostars from the respective batch (color-coded, dashed). **d** Simulated intensity enhancement (magnitude square of surface-normal electric field component) for a single nanostar with dimensions extracted from **a**. An arrow indicates the incident polarization (20 nm scale bar). **e** Schematic of the experimental setup: light is focused onto the sample (nanostars deposited on the glass substrate side facing toward the electron detector); electrons are detected using a microchannel plate (MCP) phosphor-screen assembly. **f** Photoemission map from a nanostar sample (850 nm resonance wavelength, surface density of $0.1 \mu\text{m}^{-2}$). The inset shows a fine scan over a single star, with the dashed circle indicating the FWHM intensity spot size of the laser focus (scale bar: 2 μm). **g** Scanning electron micrograph of the same region scanned in **f** (scale bar: 5 μm ; scale bar in **g** also applies to **f**). The insets show close-ups of individual nanostars (50 nm scale bars). The circles in **f** and **g** indicate the positions of nanostars leading to considerable photoemission

protuberances terminating in sharp tips, with radii as small as 4 nm (insets to Fig. 1a, b). Despite the particle-to-particle variability in the detailed nanostar morphology, the controlled growth conditions used in the synthesis allow us to tune their plasmonic response close to the laser operation wavelengths of either 660 nm (CW) or 800 nm (fs-pulses with 190 nm full-width-at-half-maximum (FWHM) spectral bandwidth). Figure 1c shows the measured ensemble optical extinction spectra for both sets of nanostars deposited on glass slides (solid curves). Electromagnetic simulations of individual nanostars (Fig. 1d) from each sample batch, with structural feature sizes extracted from the transmission electron microscope (TEM) images in Fig. 1a, b, yield spectra (dashed curves) agreeing well with the central wavelength of measured response function. The simulated spectra are essentially dominated by one of the protruding tips of the particle, and therefore, notably narrowed compared to the experimental ensemble spectra. The calculated local intensity enhancement (square of the field enhancement) exceeds 1000 at the tip region a few nanometers in diameter, as presented in Fig. 1d for a single 3D nanostar. Figure 1d plots the magnitude squared of the optical field component, which is locally perpendicular to the surface, as the surface-parallel component does not contribute significantly to photoemission due to low quantum efficiency⁴⁰. For an analysis of star ensemble effects, we refer to the study presented in ref. ², resulting essentially in broadened resonance feature.

Multiphoton photoemission. In the photoemission experiments, nanostars (Fig. 1a, b) dispensed on a fused silica substrate with conductive indium-tin-oxide (ITO) coating are illuminated with focused CW or fs-pulsed laser radiation (see “Methods” for details), as depicted in Fig. 1e. The focal spot diameters (FWHM of intensity) are $3.5 \mu\text{m} \times 1.1 \mu\text{m}$ (major \times minor axis) and $5 \mu\text{m}$ for the CW and femtosecond-pulsed illumination, respectively, enabling the excitation of single nanostars for samples with a surface coverage of $0.1 \text{ particles}/\mu\text{m}^2$. Polarization and intensity control are realized with a broadband half-wave plate and a thin-film polarizer. The photoemission measurements are conducted in a high-vacuum chamber at background pressures of 10^{-7} mbar. Emitted photoelectrons are detected using a phosphor-

screen microchannel-plate (MCP), imaged by a charge-coupled device camera for a moderate bias voltage (-10 to -30 V) applied to the sample, drawing emitted electrons toward the grounded detector front plate. Spatial photoemission maps are obtained by scanning the samples relative to the laser focus using a precision 3D translation stage.

Figure 1f, g shows a photoemission map (recorded with femtosecond excitation) and a scanning electron micrograph of the scanned region on the nanostar sample ($850 \text{ nm} \pm 100 \text{ nm}$ resonance wavelength; see Fig. 1b, c), respectively. The photoemission hotspots can be clearly identified as positions of single or multiple nanostars, indicated by the blue circles. Only particles exhibiting nanometric feature sizes (confirmed by scanning electron microscopy, see insets to Fig. 1g) yield photoemission at an incident peak intensity of 100 MWcm^{-2} . A finer scan of an individual star (see upper-right insets to Fig. 1f, g) reveals that the emission profile is significantly narrowed compared to the intensity FWHM diameter of the focal spot of the incident beam (bright emission region and dashed circle), illustrating the nonlinearity of the emission process.

The findings presented in Fig. 1f are in line with previous experiments on multiphoton photoemission from plasmonic nanostructures using femtosecond excitation^{13,15,18,21–23,41–43}. However, the observation of photoemission at peak intensities in the MWcm^{-2} range indicates the particularly high enhancement factors of these nanostars compared with nanotip structures or bow-tie antennas.

In the following, by employing the high-field enhancement in the nanostars, we demonstrate multiphoton photoemission under CW illumination with sub- MW cm^{-2} incident intensities. The nanostar sample that exhibits a resonance at $630 \text{ nm} \pm 75 \text{ nm}$ wavelength (see Fig. 1a, c) is excited with the 660-nm CW-line from a laser diode with 60 mW maximum output power. Figure 2a presents the intensity scaling (double-logarithmic plot) of the photoemission from ~ 200 nanostars in a higher-density sample (open red circles, $70 \text{ stars}/\mu\text{m}^2$) and a single nanostar of a sparse sample (open red triangles, $0.1 \text{ stars}/\mu\text{m}^2$) positioned in the CW laser focus. The photoemission from the single nanostar (verified by polarization dependence, see below) is measured at the hotspot position indicated with the arrow in the spatial scan

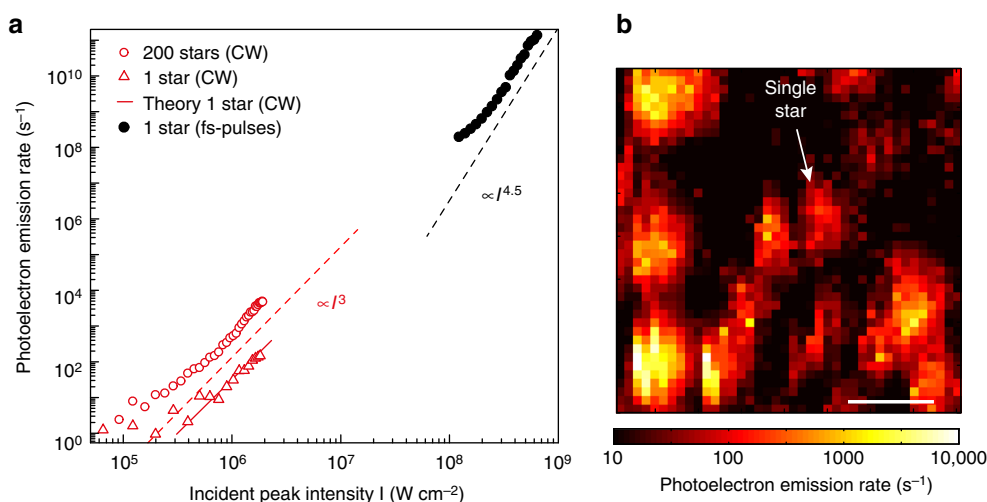


Fig. 2 Continuous-wave multiphoton photoemission. **a** Light-peak-intensity dependence of the photoelectron emission rate for single and multiple nanostars. For quantitative comparison, the photoemission rate for the femtosecond experiments is normalized to the laser duty cycle (pulse duration times repetition rate). The solid line is the calculated three-photon photoemission rate (see Eq. (1) in the “Methods” section) for a single nanostar under CW illumination, assuming an effective tip area of $5 \times 5 \text{ nm}^2$ (upper tip in Fig. 1d). The photoelectron emission rate for the experimental data is calculated from the electron count rate by assuming 10% detection efficiency of the used MCP detector. **b** Photoemission map recorded with 45 mW CW excitation, corresponding to an incident intensity of 1.5 MWcm^{-2} (scale bar: $5 \mu\text{m}$)

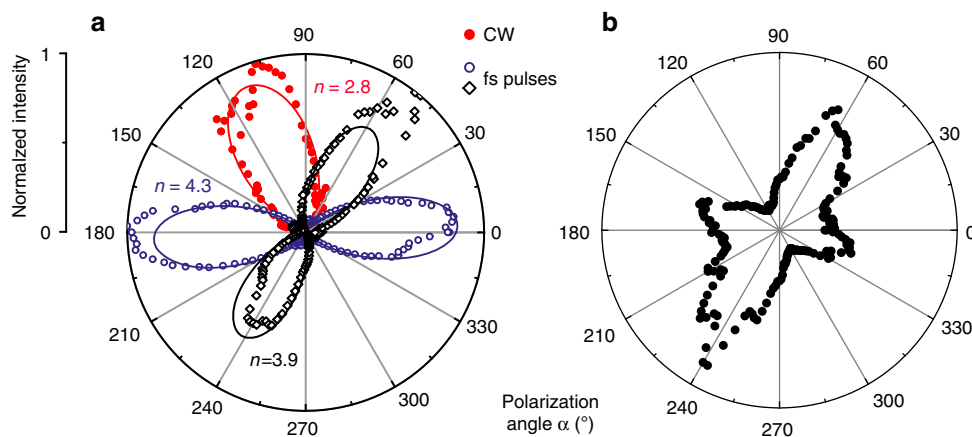


Fig. 3 Polarization dependence of photoemission from individual nanostars. **a** Measurements from three different nanostars, along with $(\cos \alpha)^{2n}$ fits (see values of n as color-coded labels) that show the nonlinear intensity dependence of the emission. (The slight asymmetry of the measured lobes likely stems from a small lateral laser focus shift caused by the rotation of the half-wave plate for polarization control and a very small wedge angle of the waveplate.) **b** Polarization-dependent femtosecond-excited photoemission from a nanostar with multiple emitting tips

of Fig. 2b. The hotspot extension and shape reflect the nonlinearity of the photoemission process and the oval shape of the focal spot, respectively. For comparison, we also plot in Fig. 2a the light-intensity-dependent photoelectron yield from a single nanostar produced upon femtosecond-pulse excitation (filled black circles). The nonlinear scalings of the photoemission signals $\propto I^n$ with incident light intensity I is indicated with dashed red ($n = 3$) and black ($n = 4.5$) lines (guides to the eye) for CW and femtosecond excitation, respectively.

In order to better understand the nonlinear photoemission process, we carry out perturbative simulations of the photoemission yield from a single nanostar under CW excitation (see solid red curve in Fig. 2a), based upon a description of conduction electrons as independent particles subject to a rectangular step potential to describe the surface barrier (see “Methods” for details). The results are in good quantitative agreement with the experimentally observed electron yield, justifying the employed perturbative treatment.

Polarization dependence. In both experiment and simulation, the far-field coupling to the resonant modes of individual nanostars strongly depends on the incident laser polarization. Figure 3a displays the polarization-dependent photoemission yields for three different stars, using either CW (solid red circles) or femtosecond-pulse (open black diamonds and blue circles) illumination. The measurements show a strong polarization dependence of the photoemission yield for each individual nanostar, thus confirming a polarization-dependent mode coupling. We find that $(\cos \alpha)^{2n}$ fits of this polarization dependence (solid curves in Fig. 3a) are generally consistent with the nonlinearity of the photoemission process for both CW ($n = 3$) and pulsed ($n = 4.5$) excitation. In the case of fs-excitation, some variation in nonlinearity for different nanostars likely stems from different resonance wavelengths overlapping the broad spectrum of the Titan:Sapphire laser (690–880 nm bandwidth) used, as well as local variations of the gold work function due to substrate effects, crystalline facets, or the nanometric size of the features^{44–46}. Somewhat higher than expected nonlinear power scalings of photoelectron yields from gold (with $n = 4–5$) have also been observed previously, for example, at sharp gold tips using 800-nm fs-excitation¹⁵. For some nanostars, we have also observed photoemission signals for more than just one polarization angle, indicating that multiple protruding tips of the nanostar can emit photoelectrons (see Fig. 3b).

Discussion

In conclusion, we demonstrated three-photon photoemission from individual gold nanoparticles using low-power CW laser radiation at a wavelength of 660 nm (1.88 eV photon energy). This type of nonlinear processes requires large light intensities typically realized by employing ultrafast laser pulses. Instead, by harnessing a 1000-fold optical CW intensity enhancement via localized plasmons at the tips of gold nanostars, we achieve a $>10^9$ -fold total enhancement of the three-photon electron yield, which agrees with calculations from a perturbative model. The findings suggest the use of very sharp tips (>4 nm radii) as coherent electron sources in future nanoscale free electron devices for quantum electronics. Our study also shows the strong potential of this system for optical near-field enhancement with general applicability to nonlinear optics (e.g., harmonic generation, frequency conversion) and strong electron (or photoelectron) interactions with amplified optical fields for microscopy, spectroscopy, and sensing.

Methods

Photoemission experiment. Two sources are used to illuminate the samples with (i) few-femtosecond, nano-joule laser pulses having a central wavelength of 800 nm at 80 MHz repetition rate, and (ii) continuous-wave radiation at a wavelength of 660 nm from a low-budget (sub-100 €) laser diode.

Materials for nanostar synthesis. Poly(vinylpyrrolidone) (PVP, MW = 25,000) was purchased from Roth. Gold(III) chloride trihydrate (99.9%, $\text{HAuCl}_4 \cdot 3\text{H}_2\text{O}$), trisodium citrate dehydrated ($\geq 99.5\%$, $\text{C}_6\text{H}_5\text{Na}_3\text{O}_7 \cdot 2\text{H}_2\text{O}$), ethanol absolute ($\geq 99.9\%$, EtOH), and indium tin oxide (ITO)-coated glass slides (surface resistivity 8–12 Ω/sq) were obtained from Sigma-Aldrich. *N,N*-dimethylformamide ($\geq 99\%$, DMF) was acquired from Fluka. All reactants were used without further purification. Milli-Q water (18 M Ω/cm) was used in all aqueous solutions, and all the glassware was cleaned with aqua regia before usage.

Synthesis of spherical Au seeds nanoparticles. Spherical Au nanoparticles of ~ 12 nm in diameter were produced by a modification of the well-known Turkevich method^{47–51}. Briefly, Milli-Q water (500 mL) was heated to boil. After boiling had commenced, a solution of sodium citrate (11 mL, 0.1 M) was added to achieve a final citrate concentration of 2.2 mM. Boiling was continued for 10 min under vigorous stirring. After this time, 833.0 μL of an aqueous solution of HAuCl_4 (0.1 M) was added to the boiling solution and was left boiling under vigorous stirring during 30 min. A condenser was utilized to prevent the evaporation of the solvent. During this time, the color of the solution gradually changed from colorless to purple to finally become deep red. The resulting particles were coated with negatively charged citrate ions, and hence, were well suspended in H_2O . Next, after cooling, the particles were added drop by drop under stirring to a previously sonicated (30 min) aqueous solution of PVP (500 mL, 0.27 mM). To guarantee that adsorption was complete, the reaction mixture was stirred for 24 h at room temperature. Finally, the Au NPs were centrifuged (9000 rpm, 35 min) and redispersed

(all in a total volume of 50 mL) in EtOH to achieve a final Au concentration of 16.2×10^{-4} M.

Synthesis of Au nanostars with λ_{\max} at 850 nm. Au nanostars were prepared by a modification of a previously reported procedure² by dissolving 6.99 g of PVP in DMF (25 mL). After its complete dissolution, 10 mL extra of DMF were added, and the mixture was further sonicated for 30 min to assure homogeneity of the polymer in the solution. Followed by the addition of an aqueous solution of HAuCl₄ (77.7 μ L, 0.1402 M) under rapid stirring at room temperature. Immediately after, 300 μ L of the preformed dispersion of 12 nm, PVP-coated Au seeds in ethanol ([Au] = 16.2×10^{-4} M) was rapidly added. Within 15 min, the color of the solution changed from pink to blue, indicating the formation of Au nanostars. The solution was left under stirring overnight to assure the reduction of all reactants. DMF and excess of PVP was removed by several centrifugation steps, a first one at 7500 rpm for 40 min followed by two more at 7000 rpm for 10 min, in all steps the particles were resuspended in EtOH (35 mL). The obtained Au nanostars, exhibit a maximum absorbance peak at 850 nm.

Synthesis of Au nanostars with λ_{\max} at 630 nm. The previous synthesis of Au stars with λ_{\max} at 850 nm was repeated, and as before, after synthesis, the obtained Au nanostars were cleaned once by centrifugation (7500 rpm, 40 min) and redispersion in EtOH (35 mL). Next, two additions of HAuCl₄ (0.1402 M) each one of 15 μ L were injected to the Au nanostar solution under vigorous stirring with 1 h time delay between them. After 4 h, the reaction was stopped by centrifugation (2 \times 7000 rpm, 10 min) and redispersion in EtOH (45 mL). The obtained Au nanostars exhibit a maximum absorbance peak at 630 nm.

ITO substrate preparation. One-side-coated ITO square glass slides (L \times W \times thickness = 25 mm \times 25 mm \times 1.1 mm) were bought and coated with 100 nm ITO on the non-coated glass side by sputtering at 150 W during 425 s.

Au nanostars substrate deposition. Both types of Au nanostars (850 nm and 630 nm) were extra cleaned by fourfold centrifugation (7000 rpm, 10 min) and redispersion in EtOH. After that, two sets of solutions for each type of stars were prepared with final Au concentrations of 8×10^{-5} M, 8×10^{-4} M, and 8×10^{-2} M. Next, 50 μ L of each concentration were spin coated (first ramp at 500 rpm for 10 s; second ramp at 3000 rpm for 30 s with an acceleration rate for both ramps of 500 rpm/s) on ITO-coated (on both sides) glass slides to achieve particle densities of \sim 0.1, 1.1, and 70 particles/ μ m² for the 630 nm Au stars and 0.07, 0.5, and 15 particles/ μ m² for the 850 nm Au stars.

Au nanostars deposition on SiN TEM grids. Au nanostars were deposited on a TEM SiN grid via spin coating (5 μ L; first ramp at 500 rpm for 10 s; second ramp at 3000 rpm for 30 s with an acceleration rate for both ramps of 500 rpm/s) from two different Au concentrations (8×10^{-5} M, 4×10^{-4} M) to achieve particle densities of 0.18 and 0.6 particles/ μ m².

Au nanostars deposition on glass slides for solid UV-VIS characterization. Solutions of both types of Au nanostars with concentrations of 5×10^{-4} M were prepared and spin-coated (50 μ L, 500 rpm, 60 s) on microscope cover-slip glass slides to achieve a low particle density sufficient to avoid interparticle coupling while enabling UV-vis spectra to be recorded.

Optical characterization. UV-VIS spectroscopy was recorded with a PerkinElmer, Lambda 19. Size, shape, and topographical characterization of the nanoparticles and the substrates were performed with transmission and scanning electron microscopy (TEM, LEO 922 EFTEM operating at 200 kV and LEO 1530 FE-SEM, Zeiss).

Electromagnetic simulations. Extinction spectra and near-field distributions are calculated using a finite-difference method (COMSOL) to solve Maxwell's equations under external plane-wave illumination for characteristic nanostar morphologies (see Fig. 1d). The dielectric function of gold is taken from optical data⁵². We note that we use a local description of the material, in which the plasmon-induced charge is fully placed in an infinitesimally thin layer at the metal surface. We neglect nonlocal effects, essentially quantified by the extension of the induced charge toward the bulk of the material over a distance (<1 nm) because this distance is small with the rounding radius of the star tips (\sim 4 nm).

Multiphoton photoemission calculation. An estimate of the photoemission rate is obtained by considering a flat surface exposed to a normal electric field with an amplitude given by the maximum intensity of the locally normal near-field resulting from the electromagnetic calculations for the nanostars. An effective hotspot area of 5×5 nm² is assumed (i.e., we multiply the electron emission current density by this area). The flat surface approximation is justified by the small electron wavelength (\sim 1 nm at the Fermi level of gold) compared with the nanostar tip rounding radius (\sim 4 nm). We describe the gold flat surface through a square-

step potential (depth $V_0 = 16.3$ eV, work function $\Phi = 4.5$ eV). Available analytical solutions⁵³ for the initial, intermediate, and final electron states are used (see detailed explicit expressions for orthonormalized wave functions in ref. 53), including their plane-wave dependence along the x - y directions parallel to the surface. As the parallel wave vector k_{\parallel} is preserved during the emission process, we study transitions involving the perpendicular wave-function components, starting from an initial state $\varphi_{n=0}(z)$ (energy $\hbar\epsilon_0$ relative to the valence band bottom), and with each of the three absorbed photons (frequency ω) producing a transition from $\varphi_{n-1}(z)$ (energy $\hbar\epsilon_0 + (n-1)\hbar\omega$) to $\varphi_n(z)$ (with $n = 1-3$). Approximating the electron-light Hamiltonian by $(-e\hbar/m\omega)[E_z(z)e^{-i\omega t} - E_z^*(z)e^{i\omega t}]\partial_z$ for an optical electric field $E_z(z)e^{-i\omega t} + E_z^*(z)e^{i\omega t}$ along the surface-normal direction z , the electron transitions under consideration can be described by iteration of the perturbative expression⁵⁴

$$\varphi_n(z) = \frac{-e\hbar}{m\omega} \int dz' G_0^+(z, z', \epsilon_0 + n\omega) E_z(z') \partial_z \varphi_{n-1}(z'), \quad (1)$$

which gives the excited wave-function component produced from φ_{n-1} , whereas

$$G_0^+(z, z', \epsilon_0 + n\omega) = \frac{m}{\hbar^2 k_n} \begin{cases} A_n e^{ik_n(z+z')} - i e^{ik_n|z-z'|}, & z, z' > 0 \\ B_n e^{ik_n z} e^{-ik_n z'}, & z > 0, z' < 0 \\ B_n e^{-ik_n z} e^{ik_n z'}, & z < 0, z' > 0 \\ \frac{k_n}{k_n} [-A_n e^{-ik_n(z+z')} - i e^{ik_n|z-z'|}], & z, z' < 0 \end{cases} \quad (2)$$

is the forward electron Green function that satisfies the identity

$$\left[-\frac{\hbar^2 \partial_z^2}{2m} + V(z) - \hbar\epsilon \right] G_0^+(z, z', \epsilon) = -\delta(z - z') \quad (3)$$

for the square-step potential $V(z)$. Here, $A_n = -i(k_n - k'_n)/(k_n + k'_n)$, $B_n = -2ik_n/(k_n + k'_n)$, $k'_n = \sqrt{2m(\epsilon + n\omega)/\hbar}$ is the electron wave vector along z inside the metal, and $k_n = \sqrt{2m(\epsilon + n\omega - V_0/\hbar)/\hbar}$ is the normal wave vector in the vacuum side. Finally, integrating over initial states (i.e., over ϵ and k_{\parallel} in the range $0 < \epsilon + \frac{\hbar k_{\parallel}^2}{2m} < E_F = V_0 - \Phi$), the photoelectron current per unit area with $n = 3$ photons (under the assumption that $\hbar n\omega > \Phi$) reduces to

$$J = \frac{e^2}{4\pi m \hbar \omega^2} \int_{k_{\min}}^{k_{\max}} \frac{dk'_0}{k_n} \left(\frac{2mE_F}{\hbar^2} - k_0'^2 \right) \times \left| \int dz \left(A_n \theta(z) e^{ik_n z} + B_n \theta(-z) e^{-ik_n z} \right) E_z(z) \partial_z \varphi_{n-1}(z) \right|^2, \quad (4)$$

where k'_0 is the initial electron wave vector inside gold, $k'_{\min} = \text{Re} \left\{ \sqrt{\frac{2mV_0}{\hbar^2} - \frac{2m\mu\omega}{\hbar}} \right\}$, and $k'_{\max} = \sqrt{2mE_F}/\hbar$.

Data availability. The data sets generated during and/or analyzed during the current study are available from the corresponding author on reasonable request.

Received: 17 November 2017 Accepted: 26 March 2018

Published online: 19 April 2018

References

- Nie, S. & Emory, S. R. Probing single molecules and single nanoparticles by surface-enhanced raman scattering. *Science* **275**, 1102–1106 (1997).
- Rodríguez-Lorenzo, L. et al. Zeptomol detection through controlled ultrasensitive surface-enhanced raman scattering. *J. Am. Chem. Soc.* **131**, 4616–4618 (2009).
- Kühn, S., Håkanson, U., Rogobete, L. & Sandoghdar, V. Enhancement of single-molecule fluorescence using a gold nanoparticle as an optical nanoantenna. *Phys. Rev. Lett.* **97**, 017402 (2006).
- Simon, H. J., Mitchell, D. E. & Watson, J. G. Optical second-harmonic generation with surface plasmons in silver films. *Phys. Rev. Lett.* **33**, 1531–1534 (1974).
- Bouhelier, A., Beversluis, M., Hartschuh, A. & Novotny, L. Near-field second-harmonic generation induced by local field enhancement. *Phys. Rev. Lett.* **90**, 013903 (2003).
- Neacsu, C. C., Reider, G. A. & Raschke, M. B. Second-harmonic generation from nanoscopic metal tips: symmetry selection rules for single asymmetric nanostructures. *Phys. Rev. B* **71**, 201402 (2005).

7. Hanke, T. et al. Efficient nonlinear light emission of single gold optical antennas driven by few-cycle near-infrared pulses. *Phys. Rev. Lett.* **103**, 257404 (2009).
8. Lippitz, M., van Dijk, M. A. & Orrit, M. Third-harmonic generation from single gold nanoparticles. *Nano Lett.* **5**, 799–802 (2005).
9. Sivis, M., Duwe, M., Abel, B. & Ropers, C. Extreme-ultraviolet light generation in plasmonic nanostructures. *Nat. Phys.* **9**, 304–309 (2013).
10. Vampa, G. et al. Plasmon-enhanced high harmonic generation from silicon. *Nat. Phys.* **13**, 659–662 (2017).
11. Sivis, M., Duwe, M., Abel, B. & Ropers, C. Nanostructure-enhanced atomic line emission. *Nature* **485**, E1–E2 (2012).
12. Sivis, M. & Ropers, C. Generation and bistability of a waveguide nanoplasma observed by enhanced extreme-ultraviolet fluorescence. *Phys. Rev. Lett.* **111**, 085001 (2013).
13. Ropers, C., Solli, D. R., Schulz, C. P., Lienau, C. & Elsaesser, T. Localized multiphoton emission of femtosecond electron pulses from metal nanotips. *Phys. Rev. Lett.* **98**, 043907 (2007).
14. Schenk, M., Krüger, M. & Hommelhoff, P. Strong-field above-threshold photoemission from sharp metal tips. *Phys. Rev. Lett.* **105**, 257601 (2010).
15. Bormann, R., Gulde, M., Weismann, A., Yalunin, S. V. & Ropers, C. Tip-enhanced strong-field photoemission. *Phys. Rev. Lett.* **105**, 147601 (2010).
16. Kruger, M., Schenk, M. & Hommelhoff, P. Attosecond control of electrons emitted from a nanoscale metal tip. *Nature* **475**, 78–81 (2011).
17. Park, D. J. et al. Strong field acceleration and steering of ultrafast electron pulses from a sharp metallic nanotip. *Phys. Rev. Lett.* **109**, 244803 (2012).
18. Dombi, P. et al. Ultrafast strong-field photoemission from plasmonic nanoparticles. *Nano Lett.* **13**, 674–678 (2013).
19. Dombi, P. et al. Phenomena in surface plasmon fields. *Opt. Express* **18**, 884–886 (2010).
20. Rác, P. et al. Strong-field plasmonic electron acceleration with few-cycle, phase-stabilized laser pulses. *Appl. Phys. Lett.* **98**, 10–13 (2011).
21. Teichmann, S. M. et al. Strong-field plasmonic photoemission in the mid-IR at 1GW/cm² intensity. *Sci. Rep.* **5**, 7584 (2015).
22. Tsang, T., Srinivasan-Rao, T. & Fischer, J. Surface-plasmon field-enhanced multiphoton photoelectric emission from metal films. *Phys. Rev. B* **43**, 8870–8878 (1991).
23. Aeschlimann, M. et al. Observation of surface enhanced multiphoton photoemission from metal surfaces in the short pulse limit. *J. Chem. Phys.* **102**, 8606–8613 (1995).
24. Hommelhoff, P. et al. Field emission tip as a nanometer source of free electron femtosecond pulses. *Phys. Rev. Lett.* **96**, 077401 (2006).
25. Yanagisawa, H. et al. Optical control of field-emission sites by femtosecond laser pulses. *J. Phys. Rev. Lett.* **103**, 257603 (2009).
26. Hoffrogge, J. et al. Tip-based source of femtosecond electron pulses at 30 keV. *J. Appl. Phys.* **115**, 094506 (2014).
27. Gulde, M. et al. Ultrafast low-energy electron diffraction in transmission resolves polymer/graphene superstructure dynamics. *Science* **345**, 200–204 (2014).
28. Vogelsgang, J. et al. Ultrafast electron emission from a sharp metal nanotaper driven by adiabatic nanofocusing of surface plasmons. *Nano Lett.* **15**, 4685–4691 (2015).
29. Schröder, B., Sivis, M., Bormann, R., Schäfer, S. & Ropers, C. An ultrafast nanotip electron gun triggered by grating-coupled surface plasmons. *Appl. Phys. Lett.* **107**, 231105 (2015).
30. Müller, M., Kravtsov, V., Paarmann, A., Raschke, M. B. & Ernstorfer, R. Nanofocused plasmon-driven sub-10 fs electron point source. *ACS Photon.* **3**, 611–619 (2016).
31. Storeck, G., Vogelsgang, S., Sivis, M., Schäfer, S. & Ropers, C. Nanotip-based photoelectron microgun for ultrafast LEED. *Struct. Dyn.* **4**, 044024 (2017).
32. Yang, D. S., Mohammed, O. F. & Zewail, A. H. Scanning ultrafast electron microscopy. *Proc. Natl Acad. Sci. USA* **107**, 14993–14998 (2010).
33. Müller, M., Paarmann, A. & Ernstorfer, R. Femtosecond electrons probing currents and atomic structure in nanomaterials. *Nat. Commun.* **5**, 5292 (2014).
34. Feist, A. et al. Ultrafast transmission electron microscopy using a laser-driven field emitter: femtosecond resolution with a high coherence electron beam. *Ultramicroscopy* **176**, 63–73 (2017).
35. Li, K., Stockman, M. I. & Bergman, D. J. Self-similar chain of metal nanospheres as an efficient nanolens. *Phys. Rev. Lett.* **91**, 227402 (2003).
36. Aeschlimann, M. et al. Adaptive subwavelength control of nano-optical fields. *Nature* **446**, 301–304 (2007).
37. Alvarez-Puebla, R., Liz-Marzán, L. M. & García de Abajo, F. J. Light concentration at the nanometer scale. *J. Phys. Chem. Lett.* **1**, 2428–2434 (2010).
38. Schuller, J. A. et al. Plasmonics for extreme light concentration and manipulation. *Nat. Mater.* **9**, 193–204 (2010).
39. Morla-Folch, J., Guerrini, L., Pazos-Perez, N., Arenal, R. & Alvarez-Puebla, R. A. Synthesis and optical properties of homogeneous nanoshurikens. *ACS Photon.* **1**, 1237–1244 (2014).
40. Lompre, L. A. & Thebault, J. Intensity and polarization effects of a single 30-psec laser pulse on five-photon surface photoeffect of gold. *Appl. Phys. Lett.* **27**, 110 (1975).
41. Fecher, G. H., Schmidt, O., Hwu, Y. & Schönhense, G. J. Multiphoton photoemission electron microscopy using femtosecond laser radiation. *Electron Spectrosc.* **126**, 77–87 (2002).
42. Kubo, A. et al. Femtosecond imaging of surface plasmon dynamics in a nanostructured silver film. *Nano Lett.* **5**, 1123–1127 (2005).
43. Zu Heringdorf, F. J. M., Chelaru, L. I., Möllenbeck, S., Thien, D. & Horn-von Hoegen, H. Femtosecond photoemission microscopy. *Surf. Sci.* **601**, 4700–4705 (2007).
44. Chelvayohan, M. & Mee, C. H. B. Work function measurements on (110), (100) and (111) surfaces of silver. *J. Phys. C* **15**, 2305 (1982).
45. Bröker, B. et al. Gold work function reduction by 2.2 eV with an air-stable molecular donor layer. *Appl. Phys. Lett.* **93**, 446 (2008).
46. Zhang, Y. et al. Sensing the charge state of single gold nanoparticles via work function measurements. *Nano Lett.* **15**, 51–55 (2014).
47. Turkevich, J., Stevenson, P. C. & Hillier, J. A study of the nucleation and growth processes in the synthesis of colloidal gold. *Discuss. Faraday Soc.* **11**, 55–75 (1951).
48. Enustun, B. V. & Turkevich, J. Coagulation of colloidal gold. *J. Am. Chem. Soc.* **85**, 3317–3328 (1963).
49. Turkevich, J. Colloidal gold. Part I. *Gold Bull.* **18**, 86 (1985).
50. Turkevich, J. Colloidal gold. Part II. *Gold Bull.* **18**, 125 (1985).
51. Frens, G. Controlled nucleation for the regulation of the particle size in monodisperse gold suspensions. *Nat. Phys. Sci.* **20**, 241 (1973).
52. Johnson, P. B. & Christy, R. W. Optical constants of the noble metals. *Phys. Rev. B* **6**, 4370–4379 (1972).
53. Garcia de Abajo, F. J. & Echenique, P. M. Ion-induced electron emission in grazing ion-surface collisions. *Nucl. Instrum. Methods Phys. Res. B* **79**, 15–20 (1993).
54. Messiah, A. *Quantum Mechanics* (North-Holland, New York, 1966).

Acknowledgements

This study was supported in part by the Deutsche Forschungsgemeinschaft (DFG) within DFG-SFB755 “Nanoscale Photonic Imaging” (project C08), the Spanish Ministerio de Economía y Competitividad (MAT2017-88492-R, SEV2015-0522, CTQ2014-59808R, CTQ2017-88648R and RYC-2015-19107), the European Research Council (Marie Curie Actions FP72014-623527), the Generalitat de Catalunya (2014-SGR-480, 2014-SGR-1400, 2017-SGR-883), and Fundació Privada Cellex.

Author contributions

M.S., F.J.G.d.A., R.A.P., and C.R. designed the study, based on an idea conceived by F.J.G.d.A. N.P.-P. synthesized the gold nanostars, prepared the samples and characterized the samples microscopically and spectrally. M.S. conducted the photoemission experiments and analyzed the data. R.Y. carried out the theoretical simulations. F.J.G.d.A. worked out the photoemission theory. M.S., C.R., and F.J.G.A. wrote the manuscript with contributions from all authors.

Additional information

Competing interests: The authors declare no competing interests.

Reprints and permission information is available online at <http://npg.nature.com/reprintsandpermissions/>

Publisher's note: Springer Nature remains neutral with regard to jurisdictional claims in published maps and institutional affiliations.



Open Access This article is licensed under a Creative Commons Attribution 4.0 International License, which permits use, sharing, adaptation, distribution and reproduction in any medium or format, as long as you give appropriate credit to the original author(s) and the source, provide a link to the Creative Commons license, and indicate if changes were made. The images or other third party material in this article are included in the article's Creative Commons license, unless indicated otherwise in a credit line to the material. If material is not included in the article's Creative Commons license and your intended use is not permitted by statutory regulation or exceeds the permitted use, you will need to obtain permission directly from the copyright holder. To view a copy of this license, visit <http://creativecommons.org/licenses/by/4.0/>.

© The Author(s) 2018